ACS OMEGA

http://pubs.acs.org/journal/acsodf

Article

Impedance Spectroscopy and Dielectric Relaxation of Imidazole-Substituted Palladium(II) Phthalocyanine (ImPdPc) for Organic Solar Cells†

Radhouane Chakroun,* Bassem Jamoussi,* Bandar Al-Mur, Abdelmajid Timoumi, and Khaled Essalah

Cite This: *ACS Omega* 2021, 6, 10655−10667

Read Online

ACCESS | Metrics & More | Article Recommendations

ABSTRACT: In this study, we investigated the potential of palladium tetrakis (imidazole) phthalocyanine ($PdPc(Imz)_4$) for use as an organic semiconductor for improving the photovoltaic performance. In order to get more information about the prevailing model of the conduction mechanism (correlated barrier hopping (CBH)) for $PdPc(Imz)_4$, electrical impedance measurements were performed at different temperatures and the obtained data were simulated by the Kohlraush Williams Watt (KWW) approach. Theoretical studies (density functional theory (DFT)) were performed and molecular electrostatic potential (MEP) maps were also extracted to understand the relationship between the molecular structures and the molecular electronic structure of $PdPc(Imz)_4$ and its semiconductor properties. Furthermore, studies on the AC electrical process as a function of temperature highlighted a hopping charge transport according to an equivalent electrical circuit composed of a parallel constant-phase element (CPE), capacitance in the grain boundary layer (C_g), and resistance of the grain boundary (R_g). To improve interpretation of the results, an in-depth analysis of the behavior of the electric transport was conducted. As a result, the correlated barrier hopping (CBH) conduction mechanism was shown to be the most suitable predominant conduction mechanism.

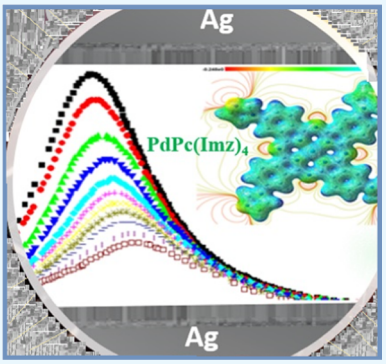

1. INTRODUCTION

In recent years, the application of organic semiconductors in microelectronics technologies has gained a new impetus due to the growing demand for low- and high-dielectric-constant materials.

Numerous reviews and articles address various aspects of the emerging semiconductor field enabling future innovations in optoelectronic devices. Some focus on the intrinsic properties of the materials, while others highlight applications such as photovoltaic cells, light-emitting diodes, and transparent transistors. Compared to these large families of materials, chalcogen-based wide-band-gap semiconductors (Ch = S, Se, Te) ($E_g > 2$ eV) are characterized by their propensity for p-type doping, high mobility, high valence-band positions, and lower ionization energies.[1−5] However, compared to M−O bonds, the weaker M−Ch (with Ch = S, Se, Te) bonds in these materials may lead to increased degradation and stability concerns in chalcogenides.[6]

Despite most of the research studies being focused on wide-band-gap inorganic materials, semiconductors are not limited to oxides and chalcogenides. Recently, several classes of organic semiconductors have been shown to have a great potential in the field of electronics and photoelectronics.

Organic semiconductors have emerged as an attractive technological alternative for large-scale power generation instead of the classic inorganic solar-cell technologies. In addition, while most inorganic solar panels require high-purity crystalline substrates, phthalocyanine-based organic solar cells (OSCs) are inexpensive, light, and can be built on a large area, without the concern of strain-induced defects.[7] Since the discovery of the semiconducting property of phthalocyanines (Pc),[7] these compounds have become one among the most used products for solar cells.[8−10]

Metallophthalocyanines (MPcs) with a lower band gap that have been widely used as electron donor material show reasonable ambipolar carrier-transporting properties for efficient charge transfer. Moreover, these compounds have been reported to be among the promising electron acceptor materials in organic solar cells (OSCs).[11]

Organic photovoltaic devices are a combination of electron donor and acceptor materials, at the interface of which a dissociation of excitons occurs (bound electron−hole pairs, formed by the absorption of a photon in the organic layer).[12] The small, macrocyclic, aromatic-copper phthalocyanine molecule (CuPc) has been shown to be a good donor layer

Received: January 4, 2021
Accepted: March 22, 2021
Published: April 16, 2021

https://doi.org/10.1021/acsomega.1c00034
ACS Omega 2021, 6, 10655−10667

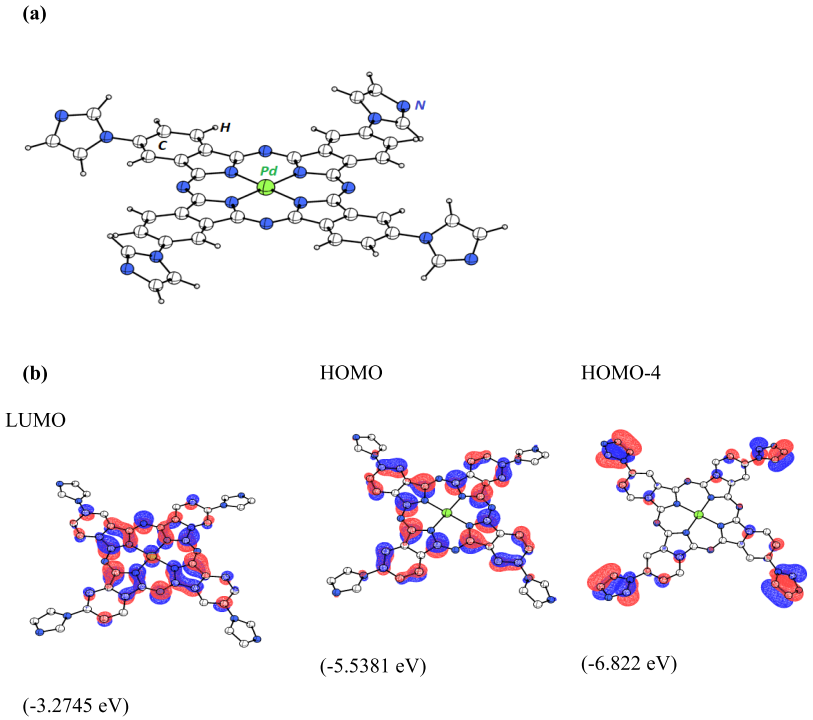

Figure 1. Theoretical analysis of $PdPc(Imz)_4$. (a) Geometry-optimized molecular model. (b) Calculated density of states (DS) for the model.

for photovoltaic devices when combined with fullerene (C60) as an acceptor material.[13] This architecture integrated the advantages of both the Schottky barrier and the donor−acceptor heterojunction in photovoltaic cells. Indeed, the Schottky barrier can provide a high Voc and the donor−acceptor heterojunction can provide more dissociation sites, which allows obtaining more photocurrent.[14]

Many studies on the modified phthalocyanine with various central metal atoms and chemical substitution have been at the focus of multidisciplinary interests ranging from photodynamic therapy in cancer treatment[15] to pigments such as the blue- and green-color filters of liquid crystal displays (LCDs),[16] and as organic thin-film transistors (OTFTs).[17] Moreover, phthalocyanines offer tremendous possibilities for the development of field-effected transistors whose charge carrier mobility greatly exceeds 1 $cm^2\ V^{-1}\ s^{-1}$,[18] an improvement in the power conversion efficiency of the solar cell larger than 5%,[19] and also for pollution monitoring as smart sensors.[20] Consequently, significant interest has been generated for the study of the electrical properties of Pc compounds and their derivatives. Khalil et al.[21] have deposited 4-tetra-4-tolylsulfonyl:zinc phthalocyanine (4T4TS:ZnPc) thin films by the spin coating technique on quartz substrates. The authors reported that the X-ray diffraction (XRD) spectra of 4T4TS:ZnPc showed a monoclinic crystalline structure in phase with a preferential orientation along (002) and ($\bar{1}$02). Indeed, in view of their efficient use in different applications, the study of the dielectric relaxation process and the electrical conductivity of these compounds has been greatly solicited. Some of the dielectric properties of PdPcs have been reported.[22−25]

In previous studies, we characterized PdPc and its derivatives deposited in the form of thin layers by vacuum evaporation and obtained encouraging results.[26−28] However, there is insufficient literature regarding the study of imidazole PdPc.

In the present paper, we report the study of the potentiality of palladium tetrakis (imidazole) phthalocyanine ($PdPc(Imz)_4$) as a donor material for new applications in electronic and photoelectronic components in solar cells. The dielectric relaxation of $PdPc(Imz)_4$ has been studied using temperature-varied complex impedance spectroscopy and the conduction mechanism has been examined by AC and DC conductivity.

2. RESULTS AND DISCUSSION

2.1. Theoretical Results of $PdPc(Imz)_4$. To give more information about the electronic features of the optimized $PdPc(Imz)_4$ compound, the electronic density plots of molecular orbitals are presented in Figure 1. In addition, E_{LUMO}, E_{HOMO}, and E_{HOMO-4} energy values of the $PdPc(Imz)_4$ compound were also calculated. In the orbits of the palladium phthalocyanine molecule, the calculated values were $E_{LUMO} = -3.2745$ eV, $E_{HOMO} = -5.5381$ eV, and $E_{HOMO-4} = -6.822$ eV.

In order to get an idea of the molecular stability, the chemical hardness (η) of $PdPc(Imz)_4$ was calculated by determination of the highest occupied molecular orbital−lowest unoccupied molecular orbital (HOMO−LUMO) energies.[29,30] To enhance the efficiency of the dye-sensitized solar cells (DSSCs), there is a need to understand the molecular behavior of $PdPc(Imz)_4$ under an electric field.[31] The global chemical reactivity descriptors of $PdPc(Imz)_4$, such as the potential (μ), the chemical hardness (η), the electronegativity (χ), and the electrophilicity power (ω) were deduced from the HOMO and LUMO energies (see Table 1).[32]

Table 1 illustrates the calculated values of the highest occupied molecular orbital energy E_{HOMO}, the lowest unoccupied molecular orbital energy E_{LUMO}, and the energy gap E_{gap} (in eV) of $PdPc(Imz)_4$. From our calculations, the E_{gap} in which the $PdPc(Imz)_4$ shows semiconductor behavior is 2.263 eV. The calculated values of the ionization potential (IP) and the electron affinity (EA) showed that $PdPc(Imz)_4$ has a very high ability for donating or accepting an electron and becoming a cation or an anion. These values are related to the low value of the energy gap ($E_{gap} = 2.263$ eV) of the compound

https://doi.org/10.1021/acsomega.1c00034
ACS Omega 2021, 6, 10655−10667

Table 1. Calculated HOMO, LUMO, Energy Gap (Δ), and Global Chemical Reactivity Descriptors

molecules' energy	6-311G
E_{LUMO}	−3.2749
E_{HOMO}	−5.5381
energy gap (Δ) $E_{HOMO} - E_{LUMO}$	2.2632
ionization potential (IP= $-E_{HOMO}$)	5.5381
electron affinity (EA = $-E_{LUMO}$)	3.2749
chemical hardness ($\eta = (I - A)/2$)	1.1316
chemical softness ($s = 1/2\eta$)	0.5658
chemical potential ($\mu = (I + A)/2$)	4.4065
electronegativity ($\chi = (1 + A)/2$)	2.1374
electrophilicity index ($\omega = \mu^2/2\eta$)	10.9862

and indicates a semiconductor behavior. Considering that there is a correlation between band gaps and bond energies, and that electronegativities come from bond energies, we may expect a correlation between the band gaps and electronegativity. Among the global descriptors of chemical reactivity, electronegativity is often used to predict the manner and direction in which materials will transport energy/electricity/heat. In addition, the value of the electrophilicity index (ω) suggests that the maximum flow of electrons between the donor and the acceptor is quite large. Furthermore, since the ionization potential of $PdPc(Imz)_4$ is 5.53 eV (Table 1) and given the Ag work function (4.35 eV),[33] we may assume the presence of a small energy barrier (SEB) of 0.18 eV at the Ag/($PdPc(Imz)_4$) interface, which is less than 0.3 eV, indicating that the transport current is due to the charge-limited currents (SCL).

The photochemical and photophysical properties of phthalocyanines depend on both central metal atoms and peripheral substitutes. The planar molecules are arranged with their planes parallel to the substrate surface. From Figure 2, we can see that there are several energies relating to the critical number of electrons corresponding to the isosurface distribution for LUMO and HOMO. The activation energy of the $PdPc(Imz)_4$ compound can be deduced from the energy difference between the Fermi level and the previous peak corresponding to the greatest number of electrons.[34] As shown in Figure 2, this value is estimated to be 0.36 eV.

In this study, molecular electrostatic potential (MEP) maps were extracted with SDD basic sets. The MEP plot of $PdPc(Imz)_4$ is characterized by a positive region (blue) at its center around the palladium atom (Figure 3a), indicating that this region is responsible for the repulsion of the proton by the atomic nuclei. The major negative region (between light brown and yellow) located on the nitrogen of the isoindole and imidazole parts of the $PdPc(Imz)_4$ compound indicates the minimum electrostatic potential (which means that there is an excess of electrons). The color ranges (in kcal/mol) from red (-4.238×10^{-2}) to blue ($+4.238 \times 10^{-2}$).

As shown in Figure 3b, the outer contour around the core is the lower isosurface and the positive charges are distributed on the exterior parts of the ligands. Since ESP highlights the negative and positive regions of a molecule, it can be said that the analysis of the electron density of $PdPc(Imz)_4$ allows us to understand the observed modifications of the electronic properties.

The electron density contours (Figure 3) show noticeable differences in the electron distribution, indicating that the core of ImPcz is the form responsible for the protonic electric conductance.

2.2. Electrical and Dielectric Properties of the $PdPc(Imz)_4$ Compound. *2.2.1. Complex Impedance Analysis.* To determine the parameters of the equivalent circuit corresponding to the $PdPc(Imz)_4$ compound, we performed a deconvolution of the Z' and Z'' curves as a function of the frequency. The simulation of the experimental data was carried out using the least-squares method based on eqs 2 and 3. The adjustment parameters were Rp, Q and α. The approximate values of the adjustable parameters were obtained as follows: Rp is the limit of Z at low frequencies and is deduced from the intersection of the representative circle of Z with the axis of the real parts on the side of the large values of Z; Q is calculated from the maximum value of Z' as a function of the frequency; $\alpha = (1 - \alpha)\pi/2$ is the angle of inclination of the segment, which passes through the origin of the reference frame and the end of the circular arc at a low frequency.

Figure 4 shows the plots of the angular frequency dependence of the impedance real part of $PdPc(Imz)_4$ at different temperatures. The amplitude of the real part Z' is higher in the region of angular frequencies <4×10^6 Hz, and decreases with increasing frequency until it becomes constant at all temperatures. Furthermore, the amplitude of the real part of impedance (Z') increases with the increasing temperature and

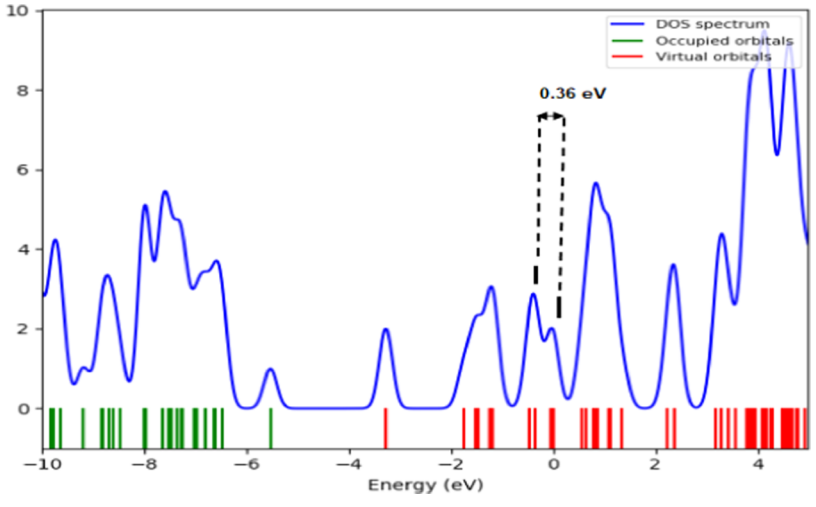

Figure 2. Isosurface distribution plot for LUMO, HOMO, and the next molecular orbital, with their corresponding energies.

https://doi.org/10.1021/acsomega.1c00034
ACS Omega 2021, 6, 10655−10667

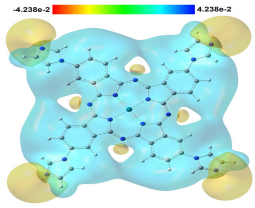

(a) Electrostatic potential from Total SCF Density (isoval = 0.025; [Mapped with ESP]).

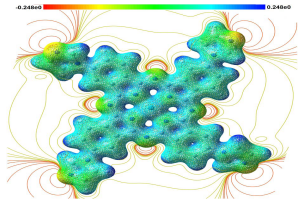

(b) Electron density from total SCF Density (isoval = 0.025); (mapped with electrostatic potential from total SCF Density and contours map.

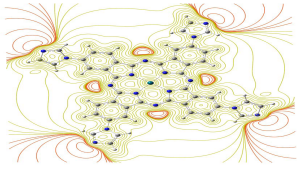

(c) Electrostatic potential from Total SCF Density (isoval = 0.025) contours in the plan of the molecule (yellow = positive ; orange = negative).

Figure 3. Electron density of $PdPc(Imz)_4$ compounds from the total SCF density (isoval = 0.025, mapped with the electrostatic potential (ESP)).

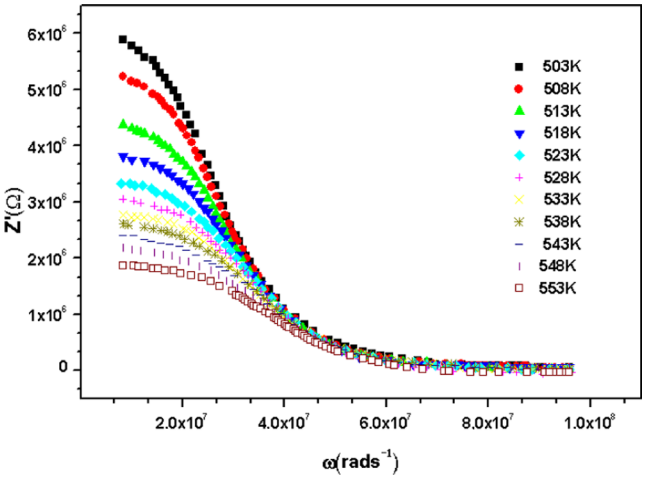

Figure 4. Variation of the real part of the impedance as a function of the angular frequency at various temperatures.

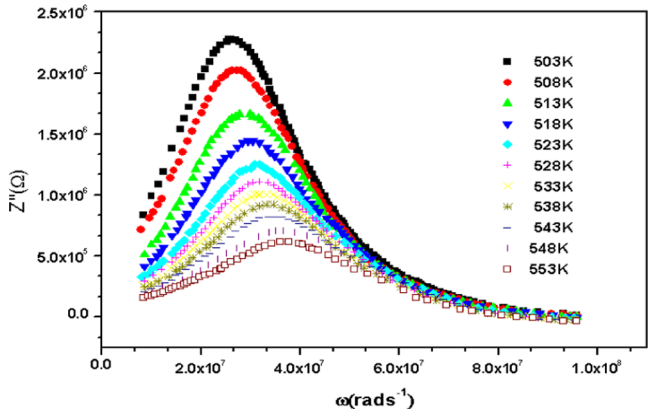

Figure 5. Variation of the imaginary part of the impedance as a function of the frequency at various temperatures.

shifts to the high-frequency side, suggesting the presence of space charge polarization in the $PdPc(Imz)_4$.[35,36] The same behavior of Z' has been previously noticed in many other phthalocyanine materials.[37] The observed temperature dependence of the actual impedance Z' may be a factor responsible for the improvement of the AC conductivity of the material with temperature at higher frequencies.[38]

Figure 5 depicts the angular frequency dependence of the impedance imaginary part Z'' of $PdPc(Imz)_4$ at various temperatures. It shows that the amplitude of Z'' increases until reaching a maximum peak (Z''_{max}), and afterward, it decreases with the increasing temperature in the same way as the frequency. The shift in the peak position corresponding to the maximum frequencies goes along with the asymmetric broadening of the loss peaks, indicating the existence of a temperature-dependent electrical relaxation phenomenon with the spread of relaxation times.[39] It is worth mentioning that the decrease of the magnitude of the imaginary impedance with the increase of the temperature, as well as the merging of all of the curves at high frequencies, indicates a possible release of the spatial charge in the material.

Figure 6 highlights a particular point of frequency around which Z'' has a maximum value and where it intersects with Z'. Moreover, when increasing the temperature from 503 to 538 K, the frequency corresponding to Z''_{max} continues to shift upward gradually from 4.058×10^6 Hz to reach 5.86×10^6 Hz. The obtained results reveal that this physical phenomenon is further

https://doi.org/10.1021/acsomega.1c00034
ACS Omega 2021, 6, 10655−10667

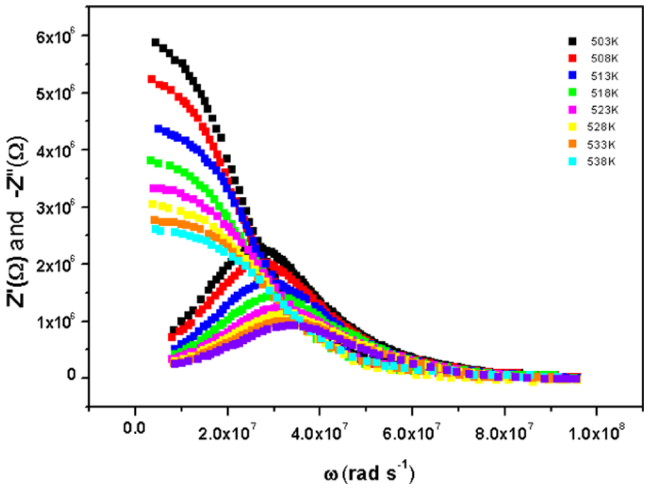

Figure 6. Frequency dependence of Z' and Z'' for $PdPc(Imz)_4$ at various temperatures.

evidence for the relaxation time distributions arising from the molecular structure of $PdPc(Imz)_4$.

2.2.2. Equivalent Circuit. As shown in Figure 7, the imaginary part of the impedance Z plotted vs its real part Z at several measurement temperatures in the range 503−553 K generates depressed semicircles. Furthermore, the decreasing radius of the arcs, which become gradually more circular with increase in the temperature, demonstrates the semiconducting nature of the phthalocyanine.[34] Most of the authors attribute this phenomenon to the Debye relaxation behavior of the grain boundaries[38] due to the nonhomogeneity of the grains, to the variations among the grain boundaries combined in series/parallel connection, and to the measured response of each individual grain boundary.

Modeling the measured impedance spectra can allow us to build an idea about the electrical equivalent circuit as well as the electrical phenomena inside the $PdPc(Imz)_4$ structure. A full semicircle with its center lying on the axis of the real part of the complex plane can be expressed in terms of a simple parallel RC equivalent circuit. In order to determine if the deviation from the ideal capacitive behavior is due to the nonhomogeneity of some properties of the system, a new constant-phase element (CPE) is introduced into the equivalent electrical circuit in place of the ideal capacitance. The explanation for the significance of the constant-phase element (CPE) has been widely discussed by Pajkossy[40] and Córdoba-Torres et al.[41] Several programming methods for computing the circuit parameters are available in the literature.[42,43] In this study, we used the *Z*-view (II) software commonly utilized for analyzing and computing electrical circuits.

The program was run over 100−500 iterations with different CPE exponents to improve the goodness of fit and get the maximum fitting. The results indicate that our data are best modeled as an active CPE circuit involving three components connected in parallel (Figure 8). The fitting parameters of the equivalent circuit at different temperatures are given in Table 2. In this study, the model of the equivalent electrical circuit obtained differs from the one proposed by Oruç et al.[39] (RC parallel circuits in series with CPEs) for phthalocyanine deposited on pure indium electrode using the thermal

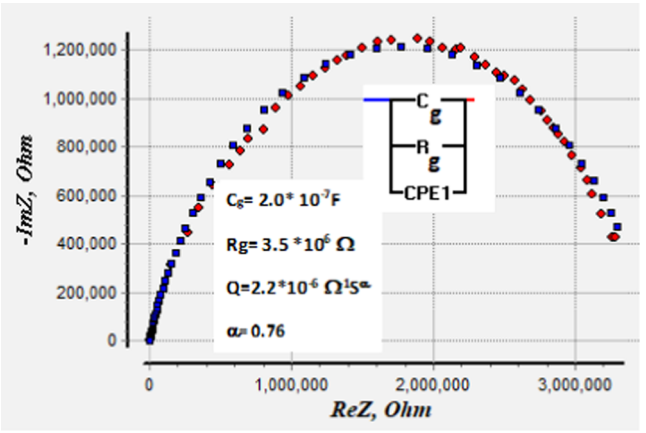

Figure 8. Cole−Cole plots at a temperature of 523 K with an electrical equivalent circuit.

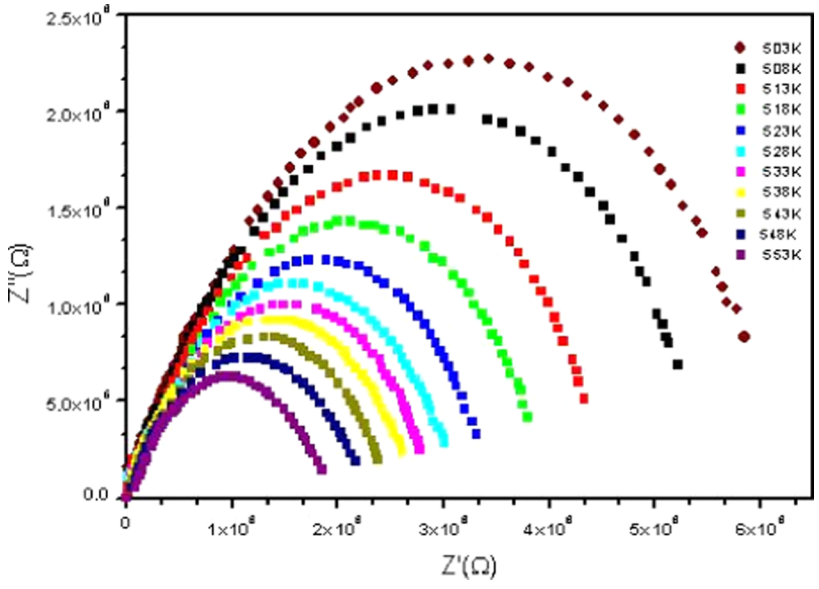

Figure 7. Cole−Cole diagrams of PdPc(Imz)4 for a range of temperatures.

https://doi.org/10.1021/acsomega.1c00034
ACS Omega 2021, 6, 10655−10667

Table 2. Values of the Parameters of the Equivalent Circuit at Different Temperatures

T (k)	R_g (Ω)	Q (Ω^{-1} s^{α})	α	C_g (F)
503	6.25×10^6	2.3×10^{-6}	0.76	2.5×10^{-7}
508	5.43×10^6	2.0×10^{-6}	0.76	2.3×10^{-7}
513	4.48×10^6	2.2×10^{-6}	0.75	2.8×10^{-7}
518	3.96×10^6	2.0×10^{-6}	0.75	2.0×10^{-7}
523	3.56×10^6	2.2×10^{-6}	0.76	2.0×10^{-7}
528	3.10×10^6	2.0×10^{-6}	0.76	2.1×10^{-7}
533	2.83×10^6	1.8×10^{-6}	0.73	1.9×10^{-7}
538	2.68×10^6	2.0×10^{-6}	0.75	2.0×10^{-7}
543	2.78×10^6	1.8×10^{-6}	0.75	2.2×10^{-7}
548	2.21×10^6	2.0×10^{-6}	0.74	2.1×10^{-7}
553	1.89×10^6	1.8×10^{-6}	0.73	2.0×10^{-7}

evaporation technique. This difference can be explained by the reduction of grain boundaries and crystalline bulk in the case of phthalocyanine in thin-film form, which reduces the resistance of the grain boundary. In the model proposed by Oruç et al.[39], the non-Debye relaxation behavior may have originated from the joints between grains, where C_g represents the capacitance of the grain boundary region.[44,45]

The impedance of the constant-phase element (CPE) is given by the relationship

$$Z_{CPE} = \frac{1}{Q(j\omega)^{\alpha}} = \frac{1}{Q\omega^{\alpha}}\left[\cos\left(\frac{\alpha\pi}{2}\right) - j\sin\left(\frac{\alpha\pi}{2}\right)\right] \quad (1)$$

where the term $Q\,[\Omega^{-1}\,s^{\alpha}]$ represents the CPE magnitude, ω ($\omega = 2\pi f$, f being the frequency) signifies the angular frequency, and $j^2 = -1$ is the imaginary number. The parameter α is related to the phase shift $\Phi = -\alpha(\pi/2)$ degrees, which is independent of the frequency.

The whole parameters of the impedance of the constant-phase element (CPE) have been evaluated by Z-view fitting according to the following equations

$$Z' = \frac{R_g^2 Q_g \omega \cos\left(\frac{\alpha_g\pi}{2}\right) + R_g}{\left(R_g Q_g \omega^{\alpha_g}\cos\left(\frac{\alpha_g\pi}{2}\right) + 1\right)^2 + \left(R_g Q_g \omega^{\alpha_g}\sin\left(\frac{\alpha_g\pi}{2}\right)\right)^2} + \frac{\cos\left(\frac{\alpha_g\pi}{2}\right)}{Q_g\omega^{\alpha_g}} \quad (2)$$

$$-Z'' = \frac{R_g^2 Q_g \omega \sin\left(\frac{\alpha_g\pi}{2}\right) + R_g}{\left(R_g Q_g \omega^{\alpha_g}\cos\left(\frac{\alpha_g\pi}{2}\right) + 1\right)^2 + \left(R_g Q_g \omega^{\alpha_g}\sin\left(\frac{\alpha_g\pi}{2}\right)\right)^2} + \frac{\sin\left(\frac{\alpha_g\pi}{2}\right)}{Q_g\omega^{\alpha_g}} \quad (3)$$

The electrical conductivity σ_{DC} was calculated as follows

$$\sigma_{DC} = \frac{e}{Z_0 S} \quad (4)$$

where e and S represent the thickness and the area of the sample, respectively. The bulk ohmic resistance Z_0 is deduced from the complex impedance diagrams (Figure 8).

Figure 9 depicts the thermal effect on the conductivity DC, $\ln(\sigma_{DC}T)$, against the reciprocal temperature according to the equation governed by the Arrehenius law

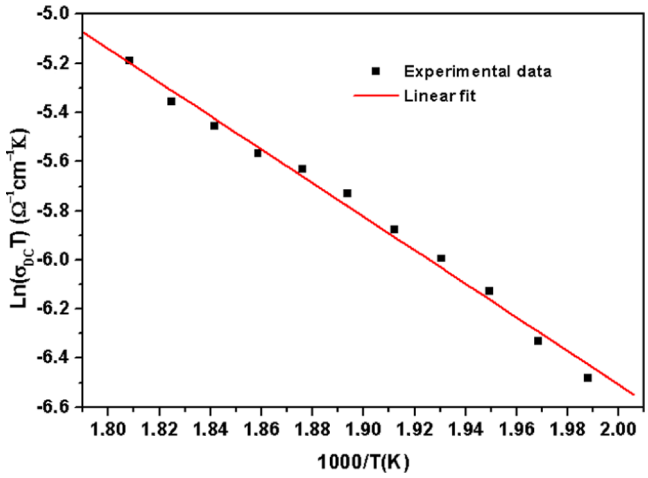

Figure 9. Variation of $\ln(\sigma_{DC}T)$ vs $1000/T$.

$$\sigma_{DC}T = A\,\exp(-E_a/k_\beta T) \quad (5)$$

where σ_{DC} is the DC conductivity, A is the pre-exponential factor, T is the absolute temperature, E_a is the apparent activation energy for the mobile ions, and k_β is the Boltzmann's constant. The activation energy deduced from the slope of the curve (Figure 9) is 0.59 eV.

2.3. Electric Modulus Study. In order to study in more detail the conduction process and/or relaxation of $PdPc(Imz)_4$, the representation of the electric modulus M^* is very useful to describe the electric conduction mechanism.

The complex electric modulus, M^*, is described in terms of the inverse of the complex permittivity ε^* as follows

$$M^* = \frac{1}{\varepsilon^*};\quad M^* = M' + jM'' = j\omega C_0 Z^* \quad (6)$$

The real M' and imaginary M'' parts of M^* have been calculated using the following relations

$$M' = \frac{\epsilon'}{\epsilon'^2 + \epsilon''^2};\quad M'' = \frac{\epsilon''}{\epsilon'^2 + \epsilon''^2} \quad (7)$$

The angular frequency dependence of M' and M'' at different temperatures for $PdPc(Imz)_4$ pellet are depicted in Figure 10a,b.

The value of the real part of the dielectric modulus M' is very small in the region of angular frequencies $\lesssim 4 \times 10^6$ Hz, but increases with increasing angular frequency at all temperatures. This tendency may be explained by the inability of the restoring force to conduct charge carrier flow to their equilibrium position under the influence of a constant electric field.[46] Instead, in the imaginary part of the electric modulus M'', there appears a broad peak that shifts toward a higher angular frequency ω_{max} ($=2\pi f_{max}$) up to a maximum peak, M''_{max}, then decreases as the temperature increases (Figure 10a). The broad shapes of the asymmetric peaks may be attributed to the phenomenon of a relaxation time distribution,[47] revealing the correlation between the motions and the mobile charge carriers.[48] Therefore, the profile of the modulus spectra confirms the existence of the hopping mechanism in the electrical conduction of the $PdPc(Imz)_4$ materials. On the other hand, the charge carrier mobility is governed by the thermally activated hopping within the localized states of the energy distribution (HOMO or LUMO) of the polypyrrole.[49] The circuit shown in Figure 8 representing a parallel combination of a resistance (R_g), a capacitance (C_g), and a fractal capacitance (CPE) confirmed the

https://doi.org/10.1021/acsomega.1c00034
ACS Omega 2021, 6, 10655−10667

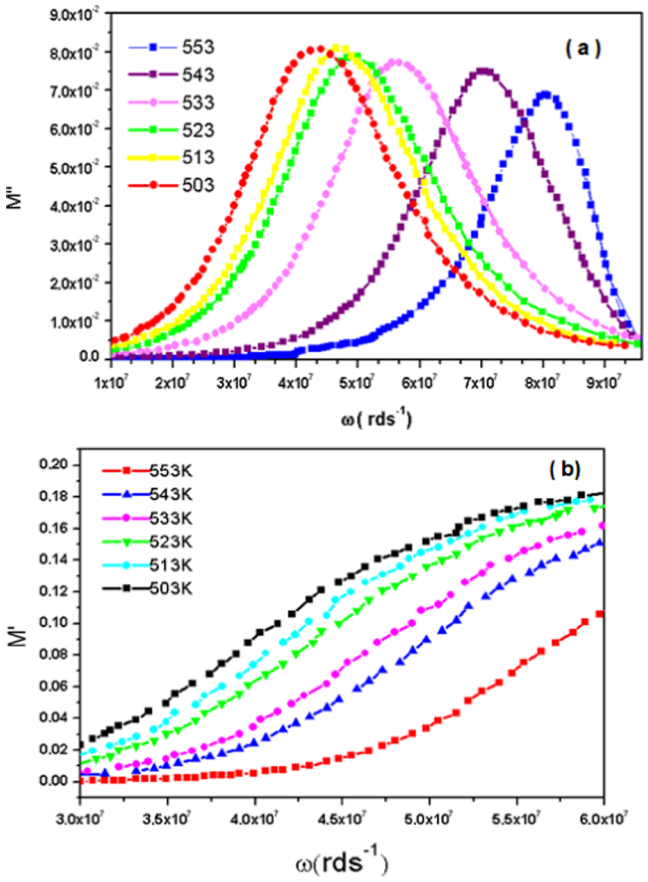

Figure 10. Frequency dependence of (a) M'' and (b) M' at different temperatures.

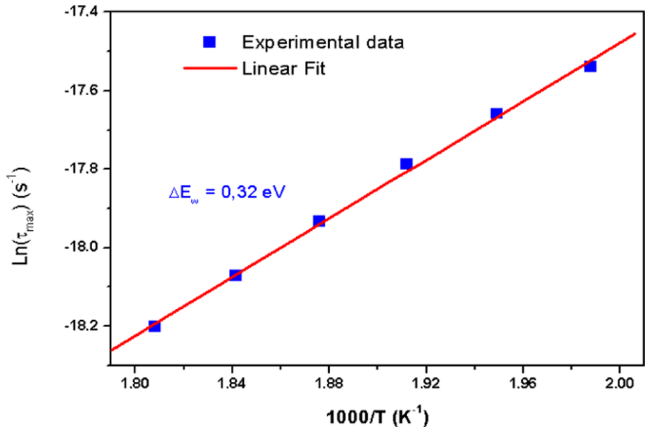

Figure 11. Arrhenius plot of the relaxation-time τ_{max} spectra.

phenomenon of the relaxation time distribution in $PdPc(Imz)_4$ pellet.

The angular frequency ω_{max}, corresponding to M''_{max}, gives the relaxation times, τ_M[47]

$$\omega_{max} = \frac{1}{\tau_M} \tag{8}$$

In addition, the shifts in the peak frequencies toward higher values with increase in the temperature is a consequence of the hopping transport. The calculated average relaxation time from Figure 10a was 1.82×10^{-8} s. For a further investigation, the temperature variation of the relaxation time τ_{max} at the maximum of M'' was studied (Figure 11) using the Arrhenius equation

$$\tau_{max} = \tau_0 \exp(\Delta E_\omega / k_B T) \tag{9}$$

where τ_0 is the pre-exponential factor and ΔE_ω is the activation energy for the electric modulus (≈0.32 eV). The observed value for the activation energy is comparable to that reported by Soliman et al.[50] for aluminum phthalocyanine chloride (AlPcCl). The authors reported an activation energy ΔE_ω = 0.34 eV.

From Figure 11, it can be seen that the activation energy calculated from the Arrhenius relation is ΔE_w = 0.32 eV. The magnitude of the activation energy suggests that the carrier transport exhibits a typical hopping conduction. Furthermore, all of the curves in Figure 10a show an asymmetric peak at the higher-frequency side. This behavior can be interpreted using Kohlraush Williams Watt (KWW) decay function, which describes the degree of deviation from the relaxation of a single charge carrier in the time domain.[51]

The complex electric modulus, M^*, against log ω plots for a certain number of ion-conducting materials is well interpreted by the Laplace transform

$$M^*(\omega) = M_\infty \left[1 - \int_0^\infty dt\ e^{i\omega t} \left(-\frac{d\varphi(t)}{dt}\right)\right] \tag{10}$$

$$\varphi(t) = \exp\left(-\left(\frac{t}{\tau_{KWW}}\right)^\beta\right) \tag{11}$$

where the exponent β $(0 < \beta < 1)$ describes the degree of non-Debye behavior, $M''_\infty = \frac{1}{\varepsilon_\infty}$ is the inverse of the dielectric constant, and τ_{KWW} represents the relaxation time of the KWW function. A new fitting approach proposed by Bergman allows a direct analysis of the frequency domain.[52] The imaginary parts $M''(\omega)$ can be written after approximation as

$$M''(\omega) = \frac{M''_{max}}{\left((1-\beta) + \left(\frac{\beta}{1-\beta}\right)\right)\left[\beta\left(\frac{\omega}{\left(\omega + \frac{\omega}{\omega_{max}}\right)^\beta}\right)\right]} \tag{12}$$

In this study, the experimental data are fitted using the modified KWW approach. The variation of the imaginary part of the normalized modulus (M''/M''_{max}) as a function of ω/ω_{max} at different temperatures is depicted in Figure 12.

An overlapping of the peak positions of the $M''(\omega)/M''$ is observed, suggesting components from both long range and localized relaxation. In this study, the Gaussian fitting of the normalized modulus peaks (Figure 13) gives a value of full width at half height (FWHH) equal to 1.78 decades (Kohlrausch parameter β = 0.64 = 1.14/FWHH). Consequently, the FWHH value is greater than the FWHH for the Debye relaxation (1.14 decades), which confirms that this relaxation follows a non-Debye-type behavior.[47]

2.4. Frequency and Temperature Dependence of AC Conductivity. The AC conductivity response of phthalocyanine has been thoroughly investigated to understand the distribution of the electric field intensity and the perturbations driven once the system is subjected to an electric field.[28,53] In this study, the AC conductivity properties and charge transport mechanism were studied on the $PdPc(Imz)_4$ pellet in the frequency and temperature ranges of 1−10 MHz and 503−553

https://doi.org/10.1021/acsomega.1c00034
ACS Omega 2021, 6, 10655−10667

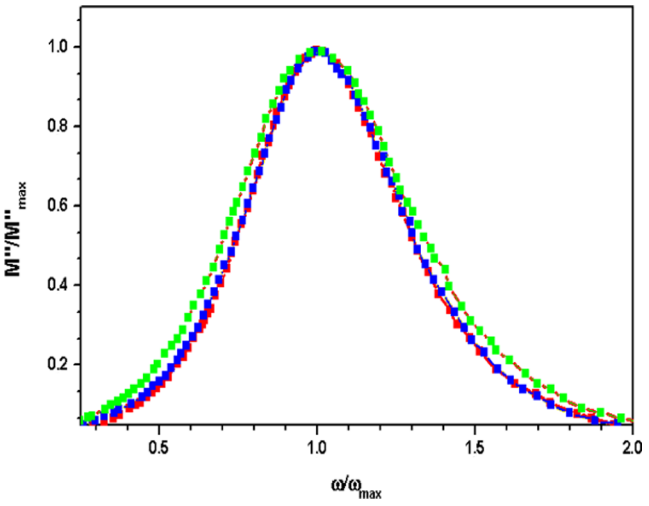

Figure 12. Frequency dependence of the normalized peaks M''/M''_{max} for the $PdPc(Imz)_4$ pellet at different temperatures.

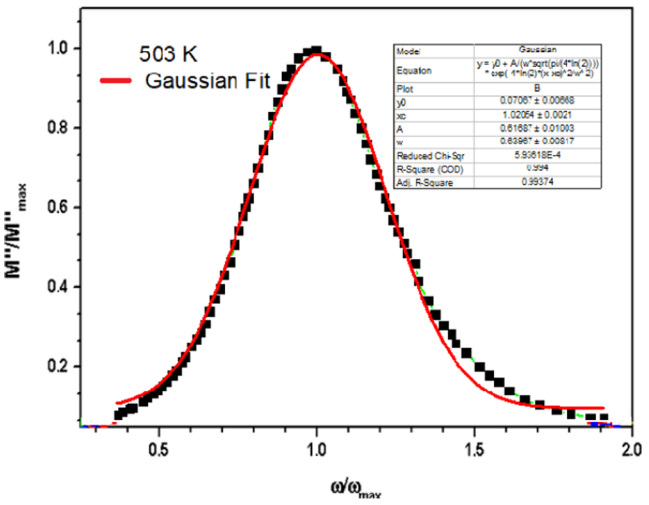

Figure 13. Gaussian fitting of the normalized modulus peaks at 503 K.

K, respectively (Figure 14). The AC electrical conductivity can be computed in accordance with the empirical relation

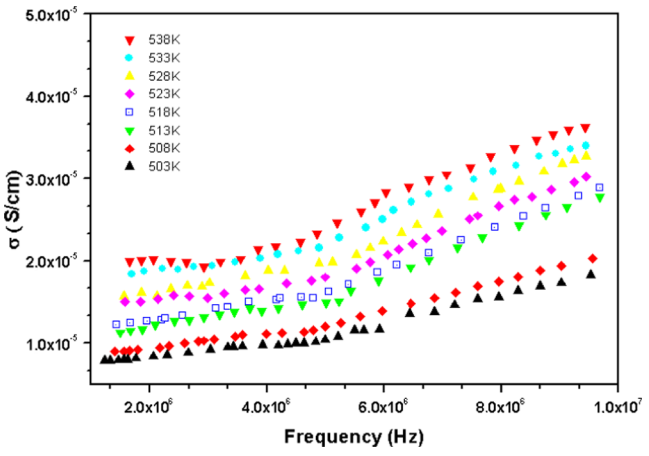

Figure 14. Frequency dependence of AC conductivity at various temperatures for the $PdPc(Imz)_4$ pellet.

$$\sigma_{ac} = \left(\frac{e}{s}\right)\left(\frac{Z'}{Z'^2 + Z''^2}\right) \quad (13)$$

where Z' and Z'' are, respectively, the real and the imaginary parts of the complex impedance, and e and σ represent, respectively, the thickness and the area of the pellet.

The behavior of the total conductivity dispersion has been introduced and analyzed by Jonscher as follows[47,54,55]

$$\sigma_{ac}(\omega) = \sigma_{dc} + A\omega^s \quad (14)$$

The equation reflects two different conduction mechanisms, represented by σ_{dc} and ω^s, where σ_{dc} is the DC conductivity (ω = 0 rad s^{-1}), A is the temperature-dependent parameter, and s is the fractional component varying between 0 and 1, characterizing the deviation from Debye behavior in the molecular system. The s values were calculated from the slope of the straight portions of the σ_{ac} vs frequency plot. A defines the strength of polarizability. The values for the exponent factor s were determined from eq 14 and the σ_{ac} (ω) vs frequency plot (Figure 14).

The variation of the AC conductivity of the $PdPc(Imz)_4$ pellet (Figure 15) shows two distinct regions (regions I and II). These

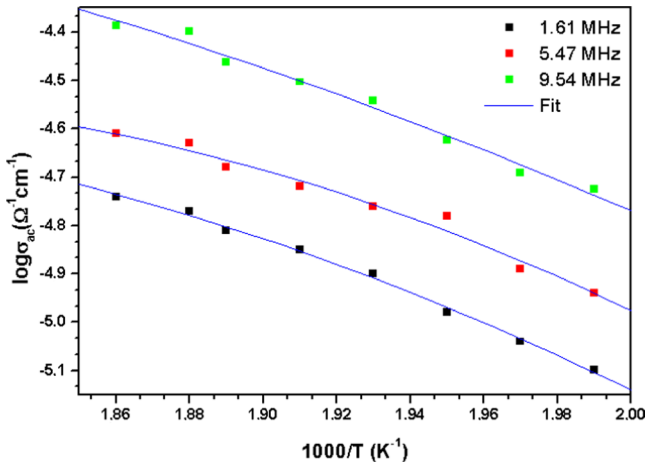

Figure 15. Plots of log $\sigma(\Omega^{-1}\ cm^{-1})$ vs $1000/T$ at different frequencies for $PdPc(Imz)_4$.

regions are referred as I (f < ~4 × 10^6 Hz), which exhibits a conductivity-independent frequency (DC conductivity region), and II (f > ~4 × 10^6 Hz), which is related to strong frequencies.

In region I, where the DC-conductivity plateau at angular frequency is less than 4.0 × 10^6 Hz, the electric field is not sufficient to perturb the charge carriers. As a result, the value of the conductivity remains nearly constant. In region II, the angular frequency is greater than 4.0 × 10^6 Hz. This region is known as the dispersive Jonscher's region, where the exponent values are between 0 and 1 (s < 1). This behavior may be expected to be due to the translational hopping motion of the charge carriers in the material.[56,57] The fitting parameters extracted using Jonscher's power law are summarized in Table 3.

These results are in good agreement with those reported in other studies, in which several metallophthalocyanine-based materials were used, such as CoPc (s = 0.7−0.8),[58] MoPc (s = 0.9),[59] MgPc (s = 0.71−0.99),[60] and Ni−$Pc(COOH)_8$ (s = 0.42−0.67).[38]

The variation of AC conductivity (ln(σAC)) as a function of temperature at three different frequencies is depicted in Figure 15. It can be seen that the conductivity of the $PdPc(Imz)_4$ pellet

https://doi.org/10.1021/acsomega.1c00034
ACS Omega 2021, 6, 10655−10667

Table 3. Values of the DC Conductance, the Constant (A), and the Exponent (s) for $PdPc(Imz)_4$

T (K)	σ_{dc} (Ω^{-1} cm^{-1})	A	exponent s
503	7.64×10^{-6}	6.19×10^{-11}	0.98
508	8.65×10^{-6}	4.51×10^{-11}	0.97
513	1.19×10^{-5}	2.91×10^{-11}	0.96
518	1.25×10^{-5}	1.75×10^{-11}	0.80
523	1.36×10^{-5}	1.19×10^{-11}	0.75
528	1.53×10^{-5}	9.53×10^{-11}	0.66
533	1.66×10^{-5}	9.56×10^{-12}	0.61
538	1.69×10^{-5}	8.17×10^{-12}	0.55

increases with increasing frequency and temperature. In addition, we can notice that E_a decreases with increasing frequency. This behavior reveals that the applied field frequency favors the electronic hopping between the localized states and consequently, the increase in AC conductivity.[61,62]

The temperature dependence of the exponent factor (s) for values less than unity is attributed to the short-distance charge hopping between the localized states. Various theoretical models for hopping were suggested under the applied AC field to elucidate the conduction mechanisms in materials, such as the quantum mechanical tunneling (QMT) model,[63] the correlated barrier hopping (CBH),[64,65] the nonoverlapping small polarons (NSPT) model,[66] and the overlapping large polaron tunneling (OLPT) model.[28,53] The temperature dependence of the extracted (s) values for the $Ag/PdPc(Imz)_4/Ag$ structure is shown in Figure 16. Among the proposed models, the present

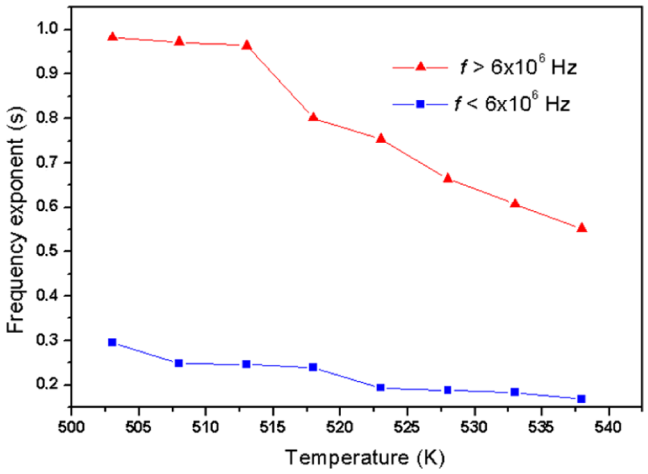

Figure 16. Thermal variation of the exponent s of $PdPc(Imz)_4$.

study showed that the exponent (s) values decrease with the increase of temperature and σ_{ac} increases with the increasing frequency (Figure 14). Therefore, the correlated barrier hopping (CBH) model[65,67] was adopted to characterize the electrical conduction mechanism of $PdPc(Imz)_4$. For this model, W_M = 0.27 eV (Figure 16). According to the CBH model, the binding energy prediction is given by the following equation[67,68]

$$s = 1 - \frac{6k_BT}{W_M - k_BT\ln(\omega\tau_0)} \quad (15)$$

where τ_0 is the characteristic relaxation time (in the order of the atom vibrational period = 10^{-13} s);[65] W_M is the binding energy; k_B is Boltzmann's constant; and ω is the angular frequency.

In Figure 16, the experimental data for frequency exponent s are fitted with the predictions of the CBH model using eq 15, and the fit of the s-curve is used to determine the value of the binding energy W_M of the carrier in its localized sites. At $503 \le T \le 538$ and $f \ge 6 \times 10^6$ Hz, the frequency exponent is close to unity. Therefore, $S \to 1$ with the increase in frequency and with the small values of $\frac{W_M}{k_BT}$. On the other hand, $S \to 0$ in the frequency range less than 6×10^6 Hz and became effectively independent of temperature. It can be pointed out that the most suitable conduction mechanism can be considered as a multiple-jumps mechanism in the frequency range $f < 2 \times 10^6$ Hz (low s values) and as single jumps for $f > 2 \times 10^6$ Hz (high s values) for the studied $PdPc(Imz)_4$ pellet. The same orders of s magnitude, corresponding to the same type of temperature dependence, have been reported by other authors for different phthalocyanine films.[69,70]

The frequency dependence of the total electrical conductivity σ_{ac} at different temperatures of the $PdPc(Imz)_4$ pellet is shown in Figure 14. From the above-mentioned results, regarding the variation of s in relation to the temperature and of the total electrical conductivity σ_{ac} in relation to frequency, we may infer that the hopping model is the most appropriate for the $PdPc(Imz)_4$ material under an electric field.

2.5. Dependence of Dielectric Constant (ε') and Loss Spectrum (ε'') on the Angular Frequency and Temperature. Most materials referred to as dielectrics exhibit three kinds of polarization, namely electronic polarization, atomic (or ionic) polarization, and orientational polarization. Nevertheless, the distortion polarization results from electronic and atomic polarization.[71,72] Figures 17 and 18 depict the frequency dependence of the dielectric constant (ε') and dielectric loss (ε'') of the $PdPc(Imz)_4$ pellet at different temperatures.

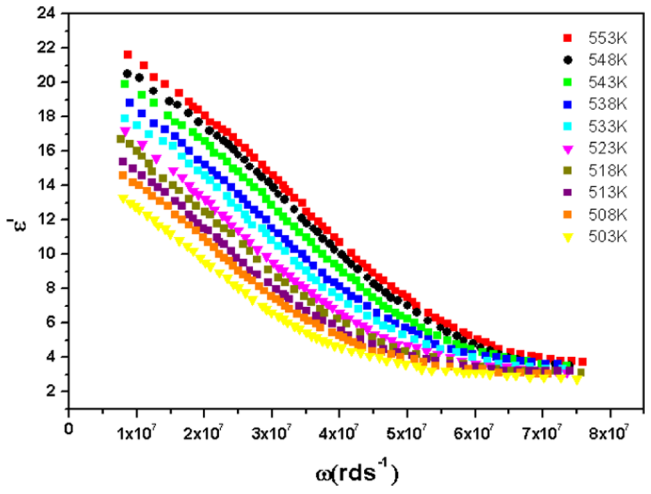

Figure 17. Dielectric constant spectra of the $PdPc(Imz)_4$ pellet at different temperatures.

The graphical plot of the real part (ε') of the complex dielectric permittivity vs angular frequency (ω) exhibits two regions. At an angular frequency of less than 4×10^7 rds^{-1}, ε' increases as ω decreases with a rapid increase at high temperatures, in agreement with the results of dielectric measurements reported for zinc and copper phthalocyanine.[73,74] On the other hand, for angular frequencies greater than 4×10^7 rds^{-1}, as the frequencies increase, the dielectric values decrease before becoming constant at ~3.4, which is the intrinsic

https://doi.org/10.1021/acsomega.1c00034
ACS Omega 2021, 6, 10655−10667

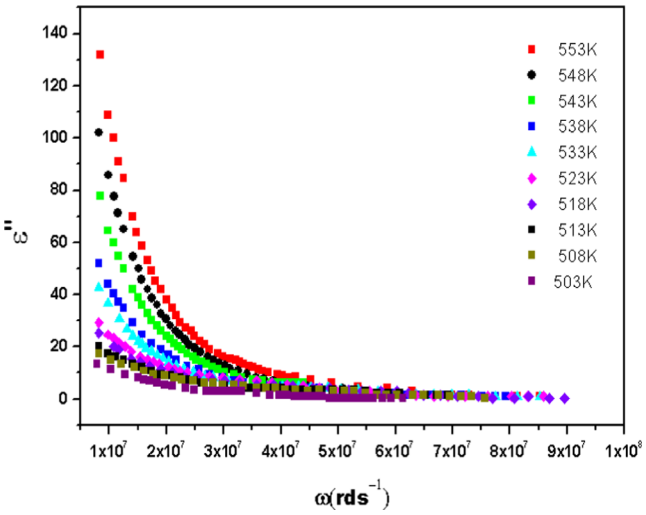

Figure 18. Dielectric loss spectra of the $PdPc(Imz)_4$ pellet at different temperatures.

dielectric constant of $PdPc(Imz)_4$. This phenomenon of decrease of the dielectric value is known as the anomalous dielectric dispersion. The dielectric constant increases as the temperature increases, which is attributed to the blocking of charge carriers at the electrodes.[73] At an angular frequency of less than 4×10^7 rds^{-1}, the same behavior was observed for ε'', which can be attributed to the contributions of the deformation and the relaxation polarization.[75] Afterward, as the frequency is increased, the value of ε'' becomes constant when reaching ~3.04. These phenomena can be explained by the strong attenuation of the rotational polarization of the molecular dipoles of $PdPc(Imz)_4$ when the frequency is increased under the effect of the electric field. Hence, the dipole orientation slows down the AC electric field due to the contribution of the deformation polarization.[75] The spectacular decrease in ε'' was widely researched for potential applications of these dielectric materials in electrical energy storage.[76−78]

3. CONCLUSIONS

In this work, a sandwiched pressed pellet of palladium tetrakis(imidazole) phthalocyanine ($PdPc(Imz)_4$), Ag/($PdPc(Imz)_4$)/Ag, was characterized by impedance spectroscopy. The SCF density shows a noticeable difference of electron distribution, suggesting that the core of ImPcz is the form responsible for the protonic electric conductance. The complex plane plots of the impedance Z at several measurement temperatures ranging from 503 to 553 K generated depressed semicircles with different radii, indicating the semiconductor property. The depressed arcs simulation of the complex Z'' as a function of the Z' plane plots indicated that the model of the equivalent circuit can be represented as a parallel combination of RC and CPE. The relaxation phenomenon has been also confirmed by the Kohlraush Williams Watt (KWW) approach. Moreover, the prevailing conduction mechanism in the $PdPc(Imz)_4$ pellet, under an AC field, can be successfully attributed to the correlated barrier hopping (CBH) model. The slope of the Arrhenius plot was determined to find the activation energy (0.56 eV). These results indicate that $PdPc(Imz)_4$ might be used as an active layer in the design of solar cells.

4. EXPERIMENTAL SECTION

4.1. Material's Synthesis. Palladium(II) tetrakis (imidazole) phthalocyanine ($PdPc(Imz)_4$) was synthesized from 4-(1*H*-imidazol-1-yl)phthalonitrile and palladium(II) acetate, in the presence of the catalyst 1,8-diazabicyclo[5.4.0]undec-7-ene (DBU) as described in previous papers.[26,27] The synthesis route is shown in Figure 19.

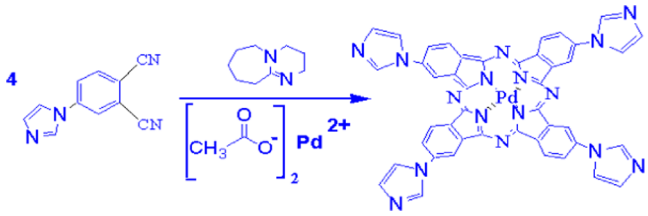

Figure 19. Palladium(II) phthalocyanine tetra-imidazole ($PdPc(Imz)_4$) synthesis.

4.2. Electrical Measurements. The electrical measurements were performed on the $PdPc(Imz)_4$ powder at room temperature under ~2900 bar by means of an hydraulic press. The pellets were obtained in the form of circular discs that were 8 mm in diameter and 2.3 mm in thickness and were painted on both sides with a conductive silver paste to behave as ohmic contacts. The complex impedance measurements were performed by a TEGAM 3550 impedance analyzer monitored by a microcomputer in the frequency range 1−10 MHz. Complex impedance measurements were carried out over the temperature range 503−553 K. The temperature was controlled using a thermocouple with 2° precision placed near the sample. The measurement results are given by the representation of the imaginary part, according to the real part of the complex impedance.[79] The software package *Z*-view was used to improve the goodness of fit and to compute the electric circuit parameters of the system.

4.3. Computational Details. Theoretical calculations of the molecular structure of $PdPc(Imz)_4$ were carried out with the density functional theory (DFT)[79] calculations using Gaussian 09[80] and Gaussian view 5.08 programs.[81] The B3LYP-GD3 hybrid density functional method has been applied to improve the description of the ground energetic state of $PdPc(Imz)_4$[82−84] using Stuttgart Dresden double ζ-effective-core potential (SDD ζ-ECPs) basis sets.[85]

AUTHOR INFORMATION

Corresponding Authors

Radhouane Chakroun − *Department of Environmental Sciences, Faculty of Meteorology, Environment and Arid Land Agriculture, King Abdulaziz University, Jeddah 21589, Saudi Arabia*; orcid.org/0000-0003-2493-9226; Phone: +96626400000; Email: rshagroon@kau.edu.sa

Bassem Jamoussi − *Department of Environmental Sciences, Faculty of Meteorology, Environment and Arid Land Agriculture, King Abdulaziz University, Jeddah 21589, Saudi Arabia*; Phone: +96626400000; Email: bissuomaj@kau.edu.sa

Authors

Bandar Al-Mur − *Department of Environmental Sciences, Faculty of Meteorology, Environment and Arid Land Agriculture, King Abdulaziz University, Jeddah 21589, Saudi Arabia*

https://doi.org/10.1021/acsomega.1c00034
ACS Omega 2021, 6, 10655−10667

Abdelmajid Timoumi − *Physics Department, Faculty of Applied Science, Umm AL-Qura University, Makkah 24381, Saudi Arabia*

Khaled Essalah − *Institut Préparatoire aux Etudes d'Ingénieurs d'El Manar, Tunis 2092, Tunisia*

Complete contact information is available at: https://pubs.acs.org/10.1021/acsomega.1c00034

Notes

The authors declare no competing financial interest.

■ ACKNOWLEDGMENTS

This project was funded by the Deanship of Scientific Research (DSR), King Abdulaziz University, Jeddah, under grant no. D-301-155-1441. The authors gratefully acknowledge the Deanship of Scientific Research (DSR), King Abdulaziz University, for technical and financial support.

■ DEDICATION

†Dedicated to the memory of Professor Faouzi Hlel.

■ REFERENCES

(1) Ojha, S.; Roy, M.; Chamuah, A.; Bhattacharya, K.; Bhattacharya, S. Transport Phenomena of Cu-S-Te Chalcogenide Nanocomposites: Frequency Response and AC Conductivity. *Phys. Chem. Chem. Phys.* **2020**, *22*, 24600−24613.

(2) Das, A. S.; Roy, M.; Roy, D.; Bhattacharya, S.; Nambissan, P.M.G. Identification of defects in the transition metal oxide-doped glass nanocomposite xV_2O_5−(1-x)(0.05MoO_3−0.95ZnO) using positron annihilation spectroscopy and other techniques. *J. Non-Cryst. Solids* **2018**, *482*, 52−62.

(3) Das, A. S.; Roy, M.; Roy, D.; Bhattacharya, S.; Nambissan, P.M.G. Defects characterization and study of amorphous phase formation in xV_2O_5-(1-x)Nd_2O_3 binary glass nanocomposites using positron annihilation and correlated experimental techniques. *J. Alloys Compd.* **2018**, *753*, 748−760.

(4) Bhattacharya, S.; Acharya, A.; Biswas, D.; Das, A. S.; Singh, L. S. Conductivity spectra of lithium ion conducting glassy ceramics. *Phys. B* **2018**, *546*, 10−14.

(5) Das, A. S.; Roy, M.; Biswas, D.; Bhattacharya, S.; Kundu, R.; Acharya, A.; et al. AC conductivity of transition metal oxide doped glassy nanocomposite systems: temperature and frequency dependency. *Mater. Res. Express.* **2018**, *5*, No. 095201.

(6) Woods-Robinson, R.; Han, Y.; Zhang, H.; Ablekim, T.; Khan, I.; Persson, K. A.; Zakutayev, A. Wide Band Gap Chalcogenide Semiconductors. *Chem. Rev.* **2020**, *120*, 4007−4055.

(7) Myers, J. D.; Xue, J. Organic Semiconductors and their Applications in Photovoltaic Devices. *Polym. Rev.* **2012**, *52*, 1−37.

(8) Islam, Z. U.; Tahir, M.; Syed, W. A.; Aziz, F.; Wahab, F.; Said, S. M.; Sarker, M. R.; Ali, S. H. M.; Sabri, M. F. M. Fabrication and Photovoltaic Properties of Organic Solar Cell Based on Zinc Phthalocyanine. *Energies* **2020**, *13*, No. 962.

(9) Urbani, M.; Ragoussi, M. E.; Nazeeruddin, M. K.; Torres, T. Phthalocyanines for dye-sensitized solar cells. *Coord. Chem. Rev.* **2019**, *381*, 1−64.

(10) Ghadari, R.; Saei, P. S.; Sabri, A.; Ghasemi, Z.; Kong, F. Enhanced phthalocyanine-sensitized solar cell efficiency via cooperation of nitrogen-doped carbon dots. *J. Cleaner Prod.* **2020**, *268*, No. 122236.

(11) Morse, G. E.; Bender, T. P. Boron subphthalocyanines as organic electronic materials. *ACS Appl. Mater. Interfaces* **2012**, *4*, 5055−5068.

(12) Gregg, B. A. Excitonic Solar Cells. *J. Phys. Chem. B* **2003**, *107*, 4688−4698.

(13) Peumans, P.; Forrest, S. R. Very-high-efficiency double-heterostructure copper phthalocyanine/C60 photovoltaic cells. *Appl. Phys. Lett.* **2001**, *79*, 126−128.

(14) Jin, F.; Su, Z.; Chu, B.; Cheng, P.; Wang, J.; Zhao, H.; Gao, Y.; Yan, X.; Li, W. Interface engineering of organic schottky barrier solar cells and its application in enhancing performances of planar heterojunction solar cells. *Sci. Rep.* **2016**, *6*, No. 26262.

(15) Ayari, S.; Saglam, M. F.; Senkuytu, E.; Ercinc, P. B.; Zorlu, Y.; Sengul, I. F.; Jamoussi, B.; Atilla, D. 3-Methylindole substituted zinc phthalocyanines for photodynamic cancer therapy. *J. Porphyrins Phthalocyanines* **2019**, *23*, 1371−1379.

(16) Choi, J.; Lee, W.; Namgoong, J. W.; Kim, T. M.; Kim, J. P. Synthesis and characterization of novel triazatetrabenzcorrole dyes for LCD color filter and black matrix. *Dyes Pigm.* **2013**, *99*, 357−365.

(17) Song, C.; Li, Y.; Gao, C.; Zhang, H.; Chuai, Y.; Song, D. An OTFT Based on Titanium Phthalocyanine Dichloride: A new p-type organic semiconductor. *Mater. Lett.* **2020**, *270*, No. 127666.

(18) Gsänger, M.; Bialas, D.; Huang, L.; Stolte, M.; Würthner, F. Organic Semiconductors based on Dyes and Color Pigments. *Adv. Mater.* **2016**, *28*, 3615−3645.

(19) De la Torre, G.; Bottari, G.; Torres, T. Phthalocyanines and Subphthalocyanines: Perfect Partners for Fullerenes and Carbon Nanotubes in Molecular Photovoltaics. *Adv. Energy Mater.* **2016**, *7*, No. 1601700.

(20) Mukherjee, D.; Manjunatha, R.; Sampath, S.; Ray, A. K. Phthalocyanines as Sensitive Materials for Chemical Sensors. In *Materials for Chemical Sensing*; Cesar Paixão, T.; Reddy, S., Eds.; Springer: Cham, 2016; pp 165−226.

(21) Khalil, S.; Tazarki, H.; Souli, M.; Guasch, C.; Jamoussi, B.; Kamoun, N. Synthesis and characterization of novel 4-Tetra-4-Tolylsulfonyl ZnPc thin films for optoelectronic applications. *Appl. Surf. Sci.* **2017**, *421*, 205−212.

(22) Jarosz, G.; Kościelska, B.; Signerski, R. Electrical properties of hybrid planar diode based on palladium phthalocyanine and titanium dioxide. *Mater. Sci.-Pol.* **2013**, *31*, 14−18.

(23) Jarosz, G. On small signal capacitance spectra of organic diode formed by ITO−palladium phthalocyanine−Al sandwich system. *Thin Solid Films* **2010**, *518*, 4015−4018.

(24) Jafari, M. J.; Azim-Araghi, M. E.; Barhemat, S. Effect of chemical environments on palladium phthalocyanine thin film sensors for humidity analysis. *J. Mater. Sci.* **2012**, *47*, 1992−1999.

(25) Parkhomenko, R. G.; Sukhikh, A. S.; Klyamer, D. D.; Krasnov, P. O.; Gromilov, S.; Kadem, B.; Hassan, A. K.; Basova, T. V. Thin films of unsubstituted and fluorinated palladium phthalocyanines: structure and sensor response toward ammonia and hydrogen. *J. Phys. Chem C* **2017**, *121*, 1200−1209.

(26) Jamoussi, B.; Chakroun, R.; Timoumi, A.; Essalah, K. Synthesis and Characterization of New Imidazole Phthalocyanine for Photodegradation of Micro-Organic Pollutants from Sea Water. *Catalysts* **2020**, *10*, No. 906.

(27) Timoumi, A.; Turkestani, M. K. A.; Alamri, S. N.; Alamri, H.; Ouerfelli, J.; Jamoussi, B. Synthesis and characterization of thin films of palladium(II) phthalocyanine and its derivatives using the thermal evaporation technique. *J. Mater. Sci.: Mater. Electron.* **2017**, *28*, 7480−7488.

(28) Timoumi, A.; Bouguila, N.; Koiab, J.; Al Turkestani, M. K.; Jamoussi, B. Study of electrical and dielectric properties of palladium-phthalocyanine (PdPc) in pellet form. *Mater. Res. Express* **2019**, *6*, No. 055103.

(29) Chen, D.; Wang, H. HOMO-LUMO energy splitting in polycyclic aromatic hydrocarbons and their derivatives. *Proc. Combust. Inst.* **2019**, *37*, 953−959.

(30) Prabhaharan, M.; Prabakaran, A. R.; Gunasekaran, S.; Srinivasan, S. DFT studies on vibrational spectra, HOMO−LUMO, NBO and thermodynamic function analysis of cyanuric fluoride. *Spectrochim. Acta, Part A* **2015**, *136*, 494−503.

(31) Urbani, M.; Ragoussi, M. E.; Nazeeruddin, M. K.; Torres, T. Phthalocyanines for dye-sensitized solar cells. *Coord. Chem. Rev.* **2019**, *381*, 1−64.

(32) Pearson, R. G. Absolute electronegativity and hardness correlated with molecular orbital theory. *Proc. Natl. Acad. Sci. U.S.A.* **1986**, *83*, 8440−8841.

(33) Mitchell, E. W. J.; Mitchell, J. W. The Work Functions of Copper, Silver and Aluminium. *Proc. R. Soc. London, Ser. A* **1951**, *210*, 70−84.
(34) Senthilarasu, S.; Sathyamoorthy, R.; Ascencio, J. A.; Lee, S. H.; Hahn, Y. B. Dielectric and ac conduction properties of zinc phthalocyanine (ZnPc) thin films. *J. Appl. Phys.* **2007**, *101*, No. 034111.
(35) Sen, S.; et al. Impedance spectroscopy study of strontium modified lead zircone titanate ceramics. *J. Appl. Phys.* **2006**, *99*, No. 124114.
(36) Suchanicz, J. The low-frequency dielectric relaxation Na0.5-Bi0.5TiO_3 ceramics. *Mater. Sci. Eng. B* **1998**, *55*, 114−118.
(37) Saad, E. A. I. Effect of phase change on dielectric properties of zinc phthalocyanine thin films. *J. Optoelectron. Adv. Mater.* **2005**, *7*, 3127−3134.
(38) Hamam, K. J.; Mezei, G.; Khattari, Z.; et al. Temperature and frequency effect on the electrical properties of bulk nickel phthalocyanine octacarboxylic acid ($NiPc(COOH)_8$). *Appl. Phys. A* **2019**, *125*, No. 7.
(39) Oruç, Ç.; Erkol, A.; Altındal, A. Characterization of metal (Ag,Au)/phthalocyanine thin film/semiconductor structures by impedance spectroscopy technique. *Thin Solid Films* **2017**, *636*, 765−772.
(40) Pajkossy, T. Impedance of Rough Capacitive Electrodes. *J. Electroanal. Chem.* **1994**, *364*, 111−125.
(41) Córdoba-Torres, P.; Mesquita, T. J.; Nogueira, R. P. Relationship between the Origin of Constant-Phase Element Behavior in Electrochemical Impedance Spectroscopy and Electrode Surface Structure. *J. Phys. Chem. C* **2015**, *119*, 4136−4147.
(42) Sarker, S.; Ahammad, A. J. S.; Seo, H. W.; Kim, D. M. Electrochemical Impedance Spectra of Dye-Sensitized Solar Cells: Fundamentals and Spreadsheet Calculation. *Int. J. Photoenergy* **2014**, *2014*, 1−17.
(43) Laajimi, M.; Chaabene, M.; Kahouech, M. S.; Ben Chaabane, R.; Jamoussi, B.; Gallot-Lavallee, O. Experimental and theoretical investigation on the effect of a spacer addition in zinc phthalocyanine-based anthracene properties. *Phys. B* **2019**, *565*, 48−60.
(44) Monama, G. R.; Hato, M. J.; Ramohlola, K. E.; Maponya, T. C.; Mdluli, S. B.; Molapo, K. M.; Modibane, K. D.; Iwuoha, E. I.; Makgopa, M. D.; Teffu, M. D. Hierarchiral 4-tetranitro copper(II)phthalocyanine based metal organic framework hybrid composite with improved electrocatalytic efficiency towards hydrogen evolution reaction. *Results Phys.* **2019**, *15*, No. 102564.
(45) El-Nahass, M. M.; Farid, A. M.; Abd El-Rahman, K. F.; Ali, H. A. M. AC conductivity and dielectric properties of bulk tin phthalocyanine dichloride ($SnPcCl_2$). *Phys. B* **2008**, *403*, 2331−2337.
(46) Haj Lakhdar, M.; Larbi, T.; Ouni, B.; Amlouk, M. AC conductivity, dielectric relaxation and modulus behavior of Sb_2S_2O new kermesite alloy for optoelectronic applications. *Mater. Sci. Semicond. Process.* **2015**, *40*, 596−601.
(47) Jonscher, A. K. Dielectric Relaxation in Solids. *J. Phys. D: Appl. Phys.* **1999**, *32*, R57−R70.
(48) Kobayashi, T.; Noguchi, Y.; Miyayama, M. Enhanced spontaneous polarization in super lattice structure $Bi_4Ti_3O_{12}$−$BaBi_4Ti_4O_{15}$ single crystal. *Appl. Phys. Lett.* **2005**, *86*, No. 012907.
(49) Somani, P.; Radhakrishnan, S. (2002). Charge transport processes in conducting polypyrrole/Prussian Blue bilayers. *Mater. Chem. Phys.* **2002**, *76*, 15−19.
(50) Soliman, I. M.; El-Nahass, M. M.; Mansour, Y. Electrical, dielectric and electrochemical measurements of bulk aluminum phthalocyanine chloride (AlPcCl). *Solid State Commun.* **2016**, *225*, 17−21.
(51) Williams, G.; Watts, D. C. Non-symmetrical dielectric relaxation behaviour arising from a simple empirical decay function. *Trans. Faraday Soc.* **1970**, *66*, 80−85.
(52) Bergman, R. General susceptibility functions for relaxations in disordered systems. *J. Appl. Phys.* **2000**, *88*, 1356−1365.
(53) Abdel-Razik, H. H. K.; Mahmoud, H. Novel Fully Conjugated 2H- and Metal-Phthalocyanine Network Polymers: Synthesis, Characterization, and Dielectric Spectra Analysis. *J. Appl. Polym. Sci.* **2012**, *123*, 1329−1339.
(54) Kao, K. C. Electrical Conduction and Photoconduction. In *Dielectric Phenomena in Solids: With Emphasis on Physical Concepts of Electronic Processes*; Elsevier Academic Press: Boston, 2004; pp 381−509.
(55) Perumal, S.; Samanta, M.; Ghosh, T.; Shenoy, U. S.; Bohra, A. K.; Bhattacharya, S.; Singh, A.; Waghmare, U. V.; Biswas, K. (2019). Realization of High Thermoelectric Figure of Merit in GeTe by Complementary Co-doping of Bi and In. *Joule* **2019**, *3*, 2565−2580.
(56) Funke, K. Jump relaxation in solid ionic conductors. *Solid State Ionics* **1988**, *28*−*30*, 100−107.
(57) Arya, S. K.; Danewalia, S. S.; Singh, K. Frequency independent low-K lithium borate nanocrystalline glass ceramic and glasses for microelectronic applications. *J. Mater. Chem. C* **2016**, *4*, 3328−3336.
(58) Abdel-Malik, T.; Kassem, M. E.; Aly, N. S.; Khalil, S. M. AC conductivity of cobalt phthalocyanine. *Acta Phys. Pol., A* **1992**, *81*, 675−680.
(59) James, S. A.; Ray, A. K.; Silver, J. Dielectric and optical studies of sublimed MoOPc films. *Phys. Status Solidi A* **1992**, *129*, 435−441.
(60) Atta, A. A. AC conductivity and dielectric measurements of bulk magnesium phthalocyanine (MgPc). *J. Alloys Compd.* **2009**, *480*, 564−567.
(61) Okutan, M.; Basaran, E.; Bakan, H. I.; Yakuphanoglu, F. AC conductivity and dielectric properties of Co-doped TiO2. *Phys. B* **2005**, *364*, 300−305.
(62) Elliott, S. R. A.c. conduction in amorphous chalcogenide and Pnictide Semiconductors. *Adv. Phys.* **1987**, *36*, 135−217.
(63) Ghosh, A. Frequency-dependent conductivity in bismuth-vanadate glassy semiconductor. *Phys. Rev. B* **1990**, *41*, 1479.
(64) Murugavel, S.; Upadhyay, M. A. C. Conduction in amorphous semiconductors. *J. Indian Inst. Sci.* **2011**, *91*, 303−317.
(65) Long, A. R. Frequency-dependent loss in amorphous semiconductors. *Adv. Phys.* **1982**, *31*, 553−637.
(66) Ghosh, A. Transport properties of vanadium germanate glassy semiconductors. *Phys. Rev. B* **1990**, *42*, 5665.
(67) Chen, R. H.; Chang, R. Y.; Shern, C. S.; et al. Impedance spectroscopy and dielectric analysis in KH_2PO_4 single crystal. *Solid State Ionics* **2006**, *177*, 2857−2864.
(68) Yakuphanoglu, F.; Aydogdu, Y.; Schatzschneider, U.; Rentschler, E. Electrical conductivity, dielectric permittivity and thermal properties of aqu[bis(2-dimethylaminomethyl-4-NT-phenolato)] of copper(II) including NaCl impurity. *Phys. B* **2003**, *334*, 443−450.
(69) Köksoy, B.; Aygün, M.; Çapkin, A.; Dumludağ, F.; Bulut, M. Electrical and gas sensing properties of novel cobalt(II), copper(II), manganese(III) phthalocyanines carrying ethyl 7-oxy-4,8-dimethylcoumarin-3-propanoate moieties. *J. Porphyrins Phthalocyanines* **2018**, *22*, 121−136.
(70) Yabaş, E.; Sülü, M.; Saydam, S.; Dumludağ, F.; Salih, B.; Bekaroğlu, Ö. Synthesis, characterization and investigation of electrical and electrochemical properties of imidazole substituted phthalocyanines. *Inorg. Chim. Acta* **2011**, *365*, 340−348.
(71) Şengül, A.; Doğan, H. Z.; Altındal, A.; Özkaya, A. R.; Salih, B.; Bekaroğlu, Ö. Synthesis, interface (Au/M2Pc2/p-Si), electrochemical and electrocatalytic properties of novel ball-type phthalocyanines. *Dalton Trans.* **2012**, *41*, 7559.
(72) Izgorodina, E. I.; Forsyth, M.; MacFarlane, D. R. On the components of the dielectric constants of ionic liquids: ionic polarization? *Phys. Chem. Chem. Phys.* **2009**, *11*, 2452.
(73) Senthilarasu, S.; Sathyamoorthy, R.; Ascencio, J. A.; Lee, S.-H.; Hahn, Y. B. Dielectric and ac conduction properties of zinc phthalocyanine (ZnPc) thin films. *J. Appl. Phys.* **2007**, *101*, No. 034111.
(74) Chen, L.; Ding, Y.; Yang, T.; Wan, C.; Hou, H. Synthesis and properties of a high dielectric constant copolymer of a copper phthalocyanine oligomer grafted to amino-capped polyimide. *J. Mater. Chem. C* **2017**, *5*, 8371−8375.
(75) Yazıcı, A.; Ünüş, N.; Altındal, A.; Salih, B.; Bekaroğlu, Ö. Phthalocyanine with a giant dielectric constant. *Dalton Trans.* **2012**, *41*, 3773.
(76) Wang, J.; Guan, F.; Cui, L.; Pan, J.; Wang, Q.; Zhu, L. Achieving high electric energy storage in a polymer nanocomposite at low filling

https://doi.org/10.1021/acsomega.1c00034
ACS Omega 2021, 6, 10655−10667

ratios using a highly polarizable phthalocyanine interphase. *J. Polym. Sci., Part B: Polym. Phys.* **2014**, *52*, 1669−1680.
(77) Li, X.; Xu, W.; Zhang, Y.; Xu, D.; Wang, G.; Jiang, Z. Chemical grafting of multi-walled carbon nanotubes on metal phthalocyanines for the preparation of nanocomposites with high dielectric constant and low dielectric loss for energy storage application. *RSC Adv.* **2015**, *5*, 51542−51548.
(78) Xie, L.; Huang, X.; Huang, Y.; Yang, K.; Jiang, P. Core@Double-Shell Structured BaTiO3−Polymer Nanocomposites with High Dielectric Constant and Low Dielectric Loss for Energy Storage Application. *J. Phys. Chem. C* **2013**, *117* (44), 22525−22537.
(79) Kohn, W.; Sham, L. J. Self-consistent equations including exchange and correlation effects. *Phys. Rev.* **1965**, *140*, A1133−A1138.
(80) Frisch, M. J.; Trucks, G. W.; Schlegel, H. B.; Scuseria, G. E.; Robb, M. A.; Cheeseman, J. R.; Scalmani, G.; Barone, V.; Mennucci, B.; Petersson, G. A.; Nakatsuji, H.; Caricato, M.; Li, X.; Hratchian, H. P.; Izmaylov, A. F.; Bloino, J.; Zheng, G.; Sonnenberg, J. L.; Hada, M.; Ehar, M. *Gaussian 09 C.01*; Gaussian Inc.: Wallingford, CT, 2010.
(81) Dennington, R.; Keith, T.; Millam, J. *GaussView*, version 5; Semichem Inc.: Shawnee Mission, KS, 2009.
(82) Becke, A. D. Density-functional exchange-energy approximation with correct asymptotic behavior. *Phys. Rev. A* **1988**, *38*, 3098−3100.
(83) Becke, A. D. Density-functional thermochemistry. III. The role of exact exchange. *J. Chem. Phys.* **1993**, *98*, 5648−5652.
(84) Lee, C.; Yang, W.; Parr, R. G. Development of the Colle-Salvetti correlation-energy formula into a functional of the electron density. *Phys. Rev. B* **1988**, *37*, 785−789.
(85) Abegg, P. W.; Ha, T. K. Ab initio calculation of spin-orbit-coupling constant from Gaussian lobe SCF molecular wave functions. *Mol. Phys.* **1974**, *27*, 763−67.

https://doi.org/10.1021/acsomega.1c00034
ACS Omega 2021, 6, 10655−10667